Catalysis Today 375 (2021) 393–400

Contents lists available at ScienceDirect

Catalysis Today

journal homepage: www.elsevier.com/locate/cattod

Supported silver catalysts prepared via melt infiltration: Synthesis, characterization and performance in selective hydrogenation

P.H. Keijzer, B. Donoeva, K.P. de Jong, P.E. de Jongh *

Inorganic Chemistry and Catalysis, Debye Institute for Nanomaterials Science, Utrecht University, Utrecht, the Netherlands

ARTICLE INFO

Keywords:
Melt infiltration
Silver
SBA-15
Nanowires
Cinnamaldehyde hydrogenation

ABSTRACT

Heterogeneous supported catalysts are often synthesized by impregnation or precipitation methods. Recently, melt infiltration has emerged as an alternative method that allows high metal loadings and eliminates the need for a solvent, but challenges arise regarding control over the particle size and distribution. In this work, melt infiltration for the synthesis of supported silver catalysts is explored. The narrow pore size distribution of the chosen ordered mesoporous silica support, SBA-15, allowed in depth *in-situ* and *ex-situ* characterization of the infiltration of the precursor, molten silver nitrate, into the support and its subsequent decomposition to form metallic silver nanowires or nanoparticles. The heat treatment parameters during decomposition played a key role in determining whether nanowires or nanoparticles were formed. The supported silver catalysts containing high silver weight loadings were investigated in the selective hydrogenation of cinnamaldehyde, where the silver nanowires showed superior activity and selectivity over the nanoparticles. Hence, melt infiltration shows great promise for the synthesis of supported silver catalysts containing high silver weight loadings, which are applicable in, e.g., selective oxidation or hydrogenation reactions.

1. Introduction

Silver catalysts are industrially used on a large scale to produce formaldehyde from methanol, and to selectively oxidize ethylene to ethylene oxide, but are also relevant for other selective oxidation and hydrogenation reactions [1–5]. If the active phase of a catalyst reside with metal nanoparticles, these are most often stabilized on a high specific surface area support material, usually a metal oxide. Porous metal oxides with an ordered pore structure and narrow pore size distribution are preferred over disordered systems for fundamental research on both the synthesis and the performance of the catalyst. One of these ordered systems is SBA-15, a mesoporous silica first synthesized by Zhao et al. [6] which has been used extensively as a model support since its discovery [7–11].

In industry mostly impregnation and precipitation are used for the synthesis of heterogenous catalysts [12–15]. For pore volume impregnation, on the one hand, the maximum weight loading is constrained by the limited solubility of precursors, and moreover, the inevitable drying step may lead to large intra- and interparticle heterogeneities in metal distribution [16–18]. Precipitation, on the other hand, allows high loadings but is accompanied by the production of large amounts of waste water [13].

For the synthesis of nanostructured materials for applications such as catalysis and batteries, melt infiltration has been proposed as an alternative method [19]. Melt infiltration makes use of capillary forces to let a liquid precursor enter a porous material spontaneously. Whether or not melt infiltration takes place depends on the degree of wetting and the related contact angle between the liquid and solid. Melt infiltration can be used for the synthesis of materials with a high weight loading. Moreover, since it is a solvent free technique, no drying step or waste water treatment is needed. However, controlling the distribution of the precursor over the support is less straightforward than when using the synthesis methods mentioned before. For example, below maximum pore filling, some pores might be completely filled, where others are empty. To prevent the uneven distribution of the precursor, the pore volume of the support can be reduced by partially filling the pores with surfactants or polymers [20,21].

There are restrictions to which precursors can be used for melt infiltration. For example, the precursor should not react with the support and only precursors that have a relative low melting temperature, at least below their decomposition temperature, can be used. Among inorganic salts, metal nitrates are particularly interesting because of

* Corresponding author.
E-mail address: P.E.deJongh@uu.nl (P.E. de Jongh).

https://doi.org/10.1016/j.cattod.2020.03.017
Received 20 November 2019; Received in revised form 4 February 2020; Accepted 12 March 2020
Available online 29 March 2020

their wide availability and easy decomposition into metal oxides. In literature, mainly metal nitrate hydrates have been reported, as of their low melting temperature resulting from dissolution of the salt in its own crystal water [19,22,23]. For several catalysts synthesized via melt infiltration using metal nitrates, the decomposition pathways are well understood, and catalyst morphology and effectiveness were reported [21,23–25]. To the best of our knowledge, this is not the case for silver nitrate, whereas the low melting temperature of silver nitrate (212 °C) in combination with its high decomposition temperature (440 °C) makes this non-hydrated metal nitrate very interesting for the melt infiltrated synthesis of high weight loading silver catalysts. Moreover, the work of Worboys et al. already shows the promise of this synthesis method, as it was reported that the pores of SBA-15 can be infiltrated with silver nitrate [26].

In this work, the use of melt infiltration for the synthesis of highly loaded silver catalysts supported on silica is described. SBA-15 was used as model support, as its narrow pore size distribution provides the opportunity to follow the infiltration process with silver nitrate using differential scanning calorimetry. After the infiltration process is complete, the decomposition of the silver nitrate into metallic silver was followed both *in-situ* and *ex-situ* using x-ray diffraction and electron microscopy, showing how the morphology of the final catalyst is influenced by the decomposition parameters. Finally, we show the application of these catalysts in the selective hydrogenation of cinnamaldehyde, where the performance is coupled to the structural properties of the catalysts.

2. Experimental

2.1. Synthesis of the support

SBA-15 was obtained via sol-gel synthesis using Pluronic P123 ($EO_{20}PO_{70}EO_{20}$, average Mw = 5800, Aldrich) as template and tetraethyl orthosilicate (TEOS, >99%, Aldrich) as silica precursor. Following the procedure of Lee et al. [27], 23.4 g Pluronic P123 was dissolved in 606.8 g deionized water and 146.4 g hydrochloric acid (HCl, 37 wt%, fuming, Merck, analysis grade) in a 1 L polypropylene bottle (cylindrical, height 19.7 cm, diameter 10.5 cm). After the mixture was vigorously stirred for at least 3 h in an oil bath at 55 °C, the stirring rate was set to 600 rpm (PFTE stirring bar, 50 x 7 mm) and 50 g TEOS was added at once. After 2 min, the stirring bar was removed and the lid of the bottle was closed tightly. The mixture was first kept for 24 h at 55 °C, then for 24 h at 90 °C. Next, the material was filtrated and washed with deionized water using a Büchner funnel until the pH of the filtrate was around 5–6 (and hence no HCl was left in the solution). The filtrate was dried at 60 °C for 2–3 days and afterwards crushed into a fine powder and calcined at 550 °C for 6 h (heating ramp 1 °C min^{-1}) in static air.

2.2. Synthesis of the catalysts

Silver was deposited on the SBA-15 via melt infiltration with silver nitrate and subsequent decomposition of the silver nitrate. In a typical synthesis, silver nitrate ($AgNO_3 \geq 99\%$, Sigma Aldrich) and SBA-15 were physically mixed in a 2:1 wt ratio inside a glovebox using a pestle and mortar for 5 min. This ratio corresponded to half of the pore volume of silica being filled with silver nitrate, resulting in a theoretical loading of 56 wt% Ag on SiO_2. The physical mixture was heated for 20 h at 250 °C under a top-down nitrogen flow (100 mL min^{-1}). The silver nitrate was decomposed by thermal treatment at 425 °C for 2 h (heating ramp of 2 °C min^{-1}) in nitrogen flow (100 mL min^{-1}) or by reduction for 2 h in 10% hydrogen in nitrogen flow (100 mL min^{-1}). This reduction either started at room temperature, whereupon the temperature was increased to 130 °C (heating ramp of 0.1 or 1 °C min^{-1}) or started at 250 °C, after prior heating in nitrogen flow. As reference, a 15 wt% Ag/SBA-15 catalyst was prepared via impregnation and drying. SBA-15 was dried under vacuum for 2 h at 250 °C prior to impregnation with an aqueous $AgNO_3$ solution (1.64 M, 90 % of pore volume). After impregnation, the composite was dried overnight under vacuum at room temperature. Next, the silver nitrate was decomposed by thermal treatment at 500 °C for 2 h (heating ramp of 1 °C min^{-1}) in static air. After cooling down, the material was reduced for 2 h at 250 °C (heating ramp of 5 °C min^{-1}) in 10 % hydrogen in nitrogen flow (100 mL min^{-1}).

2.3. Characterization

The pore size, pore volume and surface area of the synthesized SBA-15 were analyzed using N_2-physisorption. Isotherms were measured at −196 °C on a Micromeritics TriStar 3000 apparatus. The specific surface area of the support was calculated using the BET equation ($0.05 < p/p0 < 0.25$). Differential scanning calorimetry (DSC) measurements were performed on a METTLER TOLEDO HP DSC 1 system by heating the sample in a 40 µL sealed aluminum pan to 250 °C with a heating ramp of 5 °C min^{-1}, at 2 bar, under an argon flow (10 mL min^{-1}). The SBA-15, the $AgNO_3$/SBA-15 composites before and after melt infiltration and the obtained Ag/SBA-15 composites were analyzed by transmission electron microscopy (TEM) using a Tecnai20FEG and Talos F200X microscope both operated at 200 kV. For details on the surface and volume averaged particle size analysis, see Supplementary Information, Section A. TEM samples were prepared by dropwise addition of a dispersion of the material in ethanol (SBA-15 and Ag/SBA-15) or hexane ($AgNO_3$/SBA-15) obtained by sonication to a TEM grid. To prevent decomposition of the silver nitrate by the electron beam, the TEM grid with the $AgNO_3$/SBA-15 composite and grid holder were cooled with liquid nitrogen to circa −180 °C. Crystal phase analysis was performed with X-Ray Diffraction (XRD), *in-situ* on a Bruker D8 Phaser and *ex-situ* on a Bruker D2 Phaser diffractometer, both equipped with a Co Kα source (λ = 0.1789 nm). The composite structures were analyzed by comparing the XRD diffractograms with crystal structures from the PDF-4 + 2016 database. For the catalysts with a bimodal distribution of silver particles, TOPAS V5 software was used to deconvolute silver peaks into two silver phases and to calculate their crystallite sizes. Diffuse-Reflectance UV/Vis spectra of the catalysts were obtained by measuring circa 100–200 mg material in the range of 800-200 nm with a 4 nm interval and a 4 nm slit size using a Perkin Elmer Lambda 950S UV/Vis-NIR spectrophotometer with an integrating sphere detector.

2.4. Catalytic testing

The catalysts (56 wt% Ag/SiO_2) were investigated for the liquid phase hydrogenation of cinnamaldehyde. The reaction was carried out at 70 °C and under 40 bar H_2 pressure in an autoclave reactor containing 125 µL t-cinnamaldehyde, 75 mg catalyst, 100 µL tetradecane (internal standard), 6 mL isopropanol and 1 mL milliQ water. The reaction mixture was stirred at 900 rpm and samples were taken at regular time intervals of 1 or 2 h and analyzed using a Varian 430 GC.

3. Results and discussion

3.1. Melt infiltration process

The SBA-15 particles had a specific surface area of 800 m^2 g^{-1} and a well-defined pore structure with mesopores of 6.8 nm (see Supplementary Information Fig. B1). The monodisperse and ordered pore system of SBA-15 makes it possible to follow the melt infiltration process with silver nitrate by differential scanning calorimetry (DSC). With this technique, information about phase transitions of materials is obtained, as during these phase transitions, heat is released or consumed.

In Fig. 1, DSC thermograms of $AgNO_3$/SBA-15 (left frame) and macrocrystalline $AgNO_3$ (right frame) are shown. Curve A shows the measured heat flow while heating a physical mixture of silver nitrate and SBA-15 to 250 °C. Curves B and C show the same sample as in curve A, but after *in-situ* and *ex-situ* melt infiltration, respectively. The amount

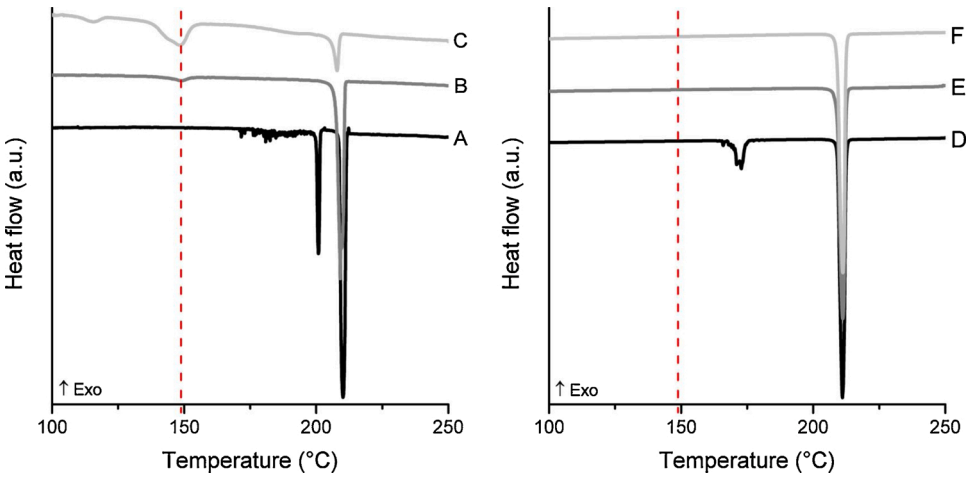

Fig. 1. DSC thermograms of $AgNO_3$/SBA-15 composites (left) and macrocrystalline $AgNO_3$ (right) recorded during heating at 5 °C min^{-1}. Curve A: physical mixture of $AgNO_3$ and SBA-15, kept at 250 °C for 4 h; curve B: second heating of composite shown in curve A; curve C: ex-situ melt infiltrated material (20 h, 250 °C, N_2 flow), curves D, E and F: first, second and third heating of macrocrystalline $AgNO_3$, respectively. Only thermograms during heating are displayed and they are offset for clarity.

of silver nitrate corresponded to 50% of the pore volume of the SBA-15. In all heating curves, including curves D–F of macrocrystalline $AgNO_3$, an endothermic peak is visible around 212 °C. In curve A, an additional endothermic peak is present at 200 °C, while in curves B and C, a second peak is observed at 148 °C.

All peaks in Fig. 1 are ascribed to phase transitions of $AgNO_3$, as in the measurement of pristine SBA-15, no peaks were observed (see Supplementary Information, Fig. B2). The endothermic peak at 200 °C in curve A is ascribed to a solid-solid phase transition of silver nitrate from the orthorhombic phase to the rhombohedral phase. X-ray diffraction (XRD) on the cooled down material confirms the transition to this rhombohedral phase and shows that the transition is irreversible (see Supplementary Information, Fig. C1). Therefore, this transition only occurred during the first heating ramp, and no peaks are visible at 200 °C in curves B and C. The solid-solid phase transition is not observed when silver nitrate was heated in the absence of silica (see Supplementary Information, Fig. C2) but has been reported before upon heating a composite of silver nitrate and silica [26].

The melting of macrocrystalline silver nitrate gave an endothermic peak at 212 °C (curves D–F), which is in agreement with literature [28]. This peak is at the same position in every thermogram of macrocrystalline $AgNO_3$ (curves D–F), while this peak slightly shifted to lower temperatures for the $AgNO_3$/SBA-15 composites in curve B and C compared to curve A. Presumably, during prior heating of materials in curves B and C in the presence of the SBA-15, the macrocrystalline silver nitrate spread out over the external surface of the SBA-15 particles, which slightly lowered the melting temperature.

By comparing the second thermogram on the $AgNO_3$/SBA-15 composite (curve B) with the second thermogram on macrocrystalline $AgNO_3$ (curve E), it becomes evident that infiltration took place. In curve E, only the peak corresponding to melting of macrocrystalline silver nitrate, at 212 °C is present, whereas in curve B, an extra peak at 148 °C is visible, which corresponds to the melting of infiltrated silver nitrate. At the start of heating curve A, the pores are empty, and therefore, only the melting of macrocrystalline silver nitrate is observed. Upon melting, part of the silver nitrate entered the pores of the SBA-15. The melting temperature of material inside nanopores is significantly lower, as a result of pore confinement [29]. Since the pores of the SBA-15 are uniform in size, the melting point depression is the same for all silver nitrate inside the pores. DSC thermograms of infiltrated material therefore show a single extra peak at lower temperature. The melting point depression of 64 °C, is close to the expected maximum decrease in melting temperature of circa 70 °C, calculated using the Gibbs-Thomson equation and assuming complete wetting, [29], see Supplementary Information, Section D. However, the low intensity of this peak and the high intensity of the peak corresponding to the melting of macrocrystalline silver nitrate indicate that most silver nitrate remained outside the pores and the *in-situ* melt infiltration is not very effective.

Curve C in Fig. 1 shows the heating of the composite after *ex-situ* melt infiltration, where the mixture was heated for 20 h at 250 °C, under nitrogen flow. The intensity of the peak of melting silver nitrate inside the pores at 148 °C is significantly higher than for curve B, while the intensity of the peak corresponding to the melting of macrocrystalline silver nitrate at 212 °C is much lower. Since the surface area of a peak corresponds directly to the amount of molten silver nitrate, a quantitative analysis on the amount of silver nitrate that infiltrated the pores is possible. From the peaks at 212 °C in curves A and C, it was calculated that 93% of the silver nitrate infiltrated the pores of the SBA-15 during the *ex-situ* melt infiltration. The higher efficiency of this *ex-situ* melt infiltration is attributed to the improved contact between the silver nitrate and the SBA-15 as result of the longer heating time.

Another method to analyze the outcome of the infiltration process is by transmission electron microscopy (TEM). With TEM, the pore structure and filling of the SBA-15 particles were imaged. In the left frame of Fig. 2, a TEM image of pristine SBA-15 is shown. With the pore structure of a SBA-15 particle aligned with the electron beam, the ordered structure became visible. The inset shows the hexagonal ordering of the pores at the end of a SBA-15 particle. The right frame of Fig. 2 shows the $AgNO_3$/SBA-15 composite (56 wt% Ag/SBA-15) after melt infiltration. Silver nitrate in an electron beam results in immediate decomposition, however, by cooling the TEM grid in liquid nitrogen, we were able to stabilize and image the silver nitrate. Here, approximately half of the pores are filled with silver nitrate and therefore, instead of bright pores, dark lines are visible within the silica structure, which confirms the successful infiltration.

3.2. Decomposition of the $AgNO_3$ precursor

After the distribution of the silver precursor over the support material, the precursor was decomposed to obtain metallic nanoparticles. For this, several methods are available, such as thermal decomposition (Eq. 1), or reduction of silver nitrate (Eq. 2). The particle size and morphology are influenced by the gas atmosphere, heating ramp and final temperature [12,30]. Using *in-situ* XRD, we followed the decomposition of silver nitrate by heating the melt infiltrated $AgNO_3$/SBA-15 composite under inert, oxidizing or reducing atmosphere up to 500 °C.

$$2\ AgNO_{3(l)} \rightarrow 2\ Ag_{(s)} + O_{2(g)} + 2\ NO_{2(g)} \quad (1)$$

$$AgNO_3 + H_{2(g)} \rightarrow Ag + H_2O + NO_{2(g)} \quad (2)$$

Fig. 3 shows the diffractograms at different temperatures, where the

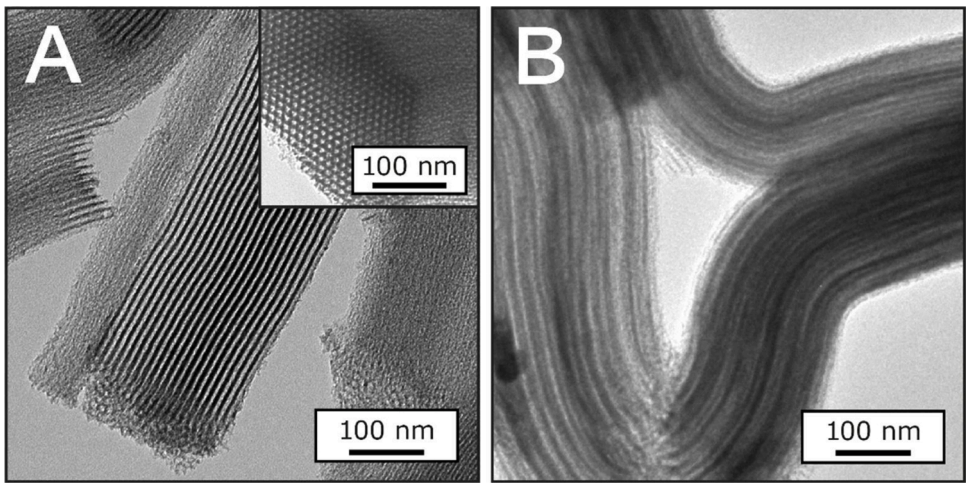

Fig. 2. TEM images of pristine SBA-15 (A) and ex-situ melt infiltrated (20 h, 250 °C, N_2 flow) $AgNO_3$/SBA-15 (B).

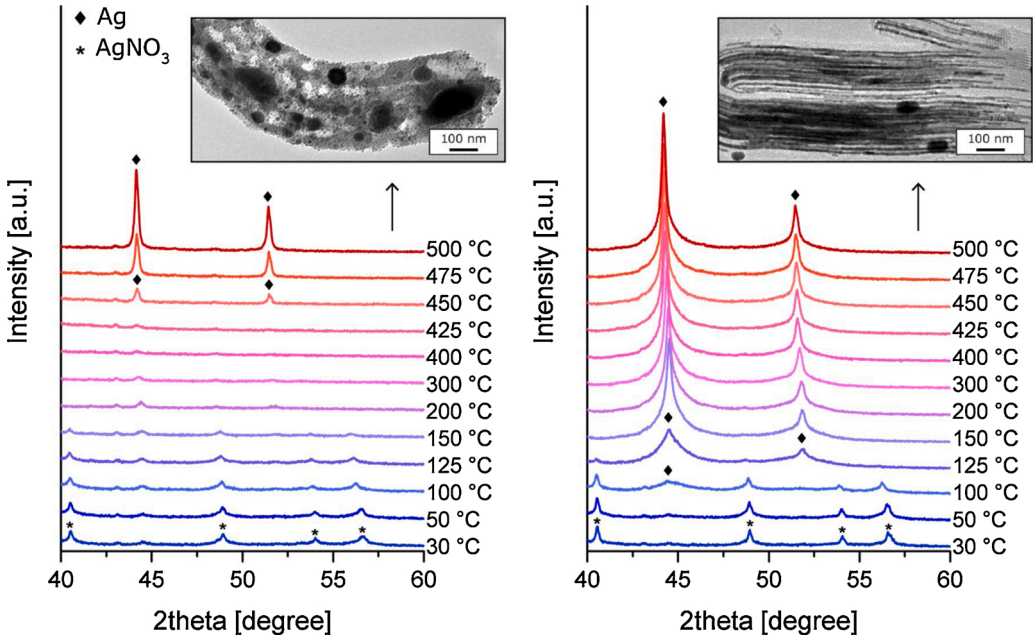

Fig. 3. In-situ XRD of melt infiltrated $AgNO_3$/SBA-15 treated in inert atmosphere (helium, left) or reducing atmosphere (5 % hydrogen in helium, right), with the inset of a TEM image of the material after heating.

left frame shows the thermal decomposition in He flow and the right frame shows its reduction in a 5% H_2 in He flow. In both graphs, peaks corresponding to silver nitrate in the rhombohedral structure are visible up to 100 °C, while large differences are observed at higher temperatures. In inert atmosphere, the peaks corresponding to silver nitrate decreased in intensity when the temperature was increased to 150 °C, and at 200 °C, crystalline phases were no longer observed. This is in line with the melting of the silver nitrate in the pores of the SBA-15, which takes place at the depressed melting temperature around 150 °C (see Fig. 1). When the composite reached 450 °C, new peaks were observed, which increased in intensity upon further heating to 500 °C. These peaks correspond to silver, indicating the decomposition of the silver nitrate into metallic silver, as is expected for macrocrystalline silver nitrate which is reported to decompose at 450 °C [28]. More in-depth analysis on the composite showed that next to the formation of silver, also some silver silicate, $Ag_{10}Si_4O_{13}$, had formed (see Supplementary Information, Fig. E1). Literature on the formation of silver silicate by reaction of silver nitrate and silica has, to the best of our knowledge, not been reported before. The liquid silver nitrate presumably reacted with the silica support at high temperature to form silver silicate and NO_x. As is visible in the TEM image of this material (Fig. 3, left frame), the pore system of the SBA-15 was completely destroyed, indicating that this silver silicate formed at the expense of the silica pore walls.

Analogous to the composite heated in inert atmosphere, the peaks in the diffractogram after heating at 30–50 °C in reducing atmosphere correspond to the rhombohedral structure of silver nitrate. However, in this case, already at 100 °C a broad peak of metallic silver appeared. The diffractograms taken at 125 °C and higher contain only peaks of metallic silver. This shows that the silver nitrate was completely reduced at 125 °C, even before melting of the silver nitrate occurred. Furthermore, no formation of silver silicate was observed, probably because of the formation of metallic silver at much lower temperature.

Fig. 4 shows TEM images of Ag/SBA-15 catalysts prepared by *ex-situ* decomposition of the infiltrated material. For more TEM images giving a larger scale overview, see Supplementary Information, Fig. E2. In frame A, silver nitrate was thermally decomposed by heating to 425 °C in

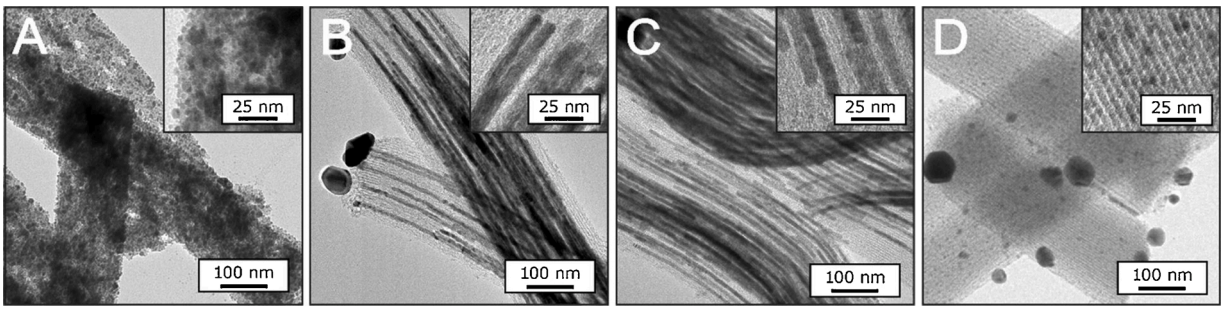

Fig. 4. Ag/SBA-15 composites after decomposition of the silver nitrate in nitrogen (A) and in 10 % hydrogen (B–D). Silver nanowires inside the pores of the SBA-15 were obtained when reduction was started at room temperature with a heating ramp of 1 °C min^{-1} (B) or 0.1 °C min^{-1} (C), while starting the reduction at 250 °C led to the formation of silver nanoparticles inside the pores (D).

nitrogen flow. Just as with the material heated during the *in-situ* XRD measurements, SBA-15 particles no longer contained ordered pores, due to the formation of silver silicate. In order to prevent the formation of silver silicate, the decomposition of the silver nitrate was in all other cases conducted under reductive atmosphere, resulting in the materials shown in Fig. 4, frames B, C and D. Silver nanowires which filled some of the pores of the SBA-15 completely, are visible in frames B and C, while small silver nanoparticles distributed over the pores are visible in frame D.

The silver nanowires were obtained by starting the reduction at room temperature by applying a flow of 10 % H_2 in N_2, and by slowly heating the composite to 130 °C in this atmosphere. Both when a heating ramp of 0.1 °C min^{-1} or 1 °C min^{-1} was used, SBA-15 with silver nanowires inside the pores were obtained. Although the heating ramp was different, the silver nanowires were very similar in both catalysts, and the pores of the SBA-15 were either completely filled, or completely empty. The similarities of these samples is further supported by the similar plasmon absorption peaks in the UV/Vis spectra, with a maximum absorption at 388 nm for both materials (see Supplementary Information, Fig. E3). Considering that volume of silver nitrate is 3.8 times larger than for metallic silver, it is striking that completely filled pores were observed. However, the formation of silver nanowires in SBA-15 has been reported before and is ascribed to the mobility of intermediate phases during the decomposition [26,30].

By altering the heat treatment parameters, the morphology of the silver was changed considerably. When the infiltrated material was first heated to 250 °C in inert atmosphere, and the reduction was started at this temperature, the pores of the SBA-15 contained silver nanoparticles of 2.3 ± 0.7 nm (Fig. 4, frame D). The silver nanoparticles were uniformly distributed over the pores. The nanoparticles show a maximum plasmonic absorption at 368 nm (see Supplementary Information, Fig. E3). The intensity of this peak is lower than for the nanowires and the peak location is at a shorter wavelength, confirming the formation of smaller silver nanoparticles. By increasing the temperature before starting the reduction, probably more nuclei were created, just as with the "hot injection" synthesis method of colloidal particles [31]. This prevented the formation of nanowires and facilitated the formation of many small nanocrystallites.

Next to TEM, XRD was used to determine the average particle size, since the width and intensity of silver peaks gives information on the crystallite size of the material [32,33]. In Fig. 5, the XRD diffractograms of the Ag/SBA-15 composites are shown, in which all peaks correspond to metallic silver (black curves). The shape of these peaks indicate the presence of a bimodal size distribution, since the broad base of the peaks suggests the presence of small crystallites, whereas the sharp tips imply larger crystallites [33]. Using TOPAS V5 software, each peak in the diffractograms was deconvoluted into two separate peaks, one sharp peak for large crystallites (red curves) and one broad peak for smaller crystallites (green curves), where the sum of these two peaks, the total fit, is in good agreement with the experimental data (see Supplementary Information, Fig. E4). In doing so, both the average crystallite sizes and the percentages of silver in each phase were estimated [34].

In Table 1, an overview of the different materials with the measured particle sizes using TEM and the calculated crystallite sizes from the deconvoluted peaks and percentages of silver present in the small crystallites are given. The calculated size of the large crystallites overlap with the size of the large silver particles on the external surface area of the SBA-15, present in all three catalysts. The small crystallite sizes obtained from the XRD data were very similar to the measured nanowire thicknesses obtained via TEM. The small crystallite size calculated in

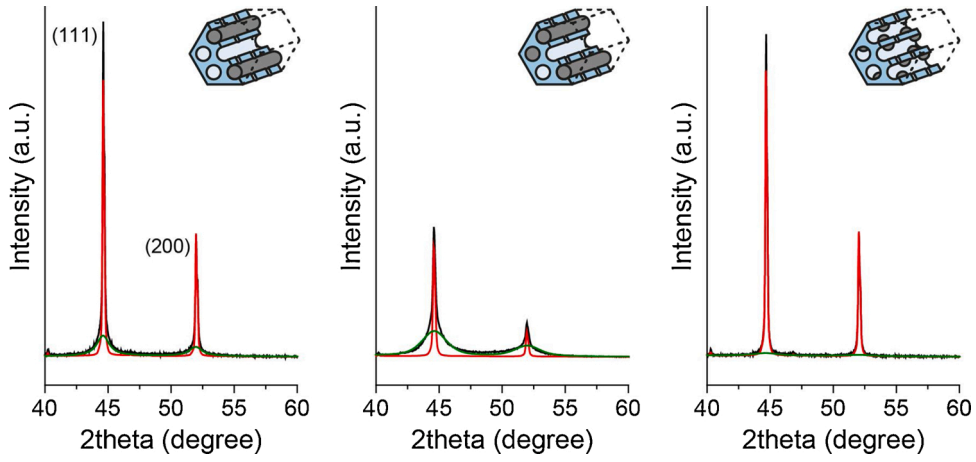

Fig. 5. XRD diffractogram of Ag/SBA-15_1 (left), Ag/SBA-15_0.1 (middle) and Ag/SBA-15_N_2 (right) in black and the deconvoluted peaks for small crystallites in green and large crystallites in red. (For interpretation of the references to colour in the Figure, the reader is referred to the web version of this article).

Table 1
Overview of particle/crystallite sizes of the Ag/SBA-15 composites.

Material	Heating ramp (°C min^{-1})	H_2 during heating (%)	Ag nanowire / nanoparticle diameter[a] (nm)	Small / large crystallite sizes[b] (nm)	Small crystallites[b] (%)	Ag surface atoms inside pores[c] (%)
Ag/SBA-15_1	1	10	10.0 ± 1.4	9.9 / 252	39	92
Ag/SBA-15_0.1	0.1	10	9.1 ± 0.9	9.7 / 150	73	97
Ag/SBA-15_N_2	2	0	2.3 ± 0.7	5.1 / 227	19	91

[a] Volume averaged sizes determined by TEM.
[b] Calculated from deconvoluted XRD peaks using TOPAS V5 software.
[c] Based on the volume averaged crystallite sizes and fractions calculated using TOPAS V5 software.

Ag/SBA-15_N_2 however, was larger than the measured nanoparticle size on TEM images. This is expected, since in the TEM image analysis, only nanoparticles in the pores were measured, while for XRD, a volume average of all smaller crystallites was taken, which includes some particles of 5–10 nm also present outside of the pores that shift the average to a higher value. Furthermore, silver nanoparticles below 2 nm give a very broad peak with a low intensity, barely visible in the diffractogram, and therefore, they are at least partly unaccounted for.

The amount of silver inside versus outside of the pores was estimated by assuming that the small crystallites were inside the pores of the SBA-15, while the larger crystallites were outside. These values are given in Table 1 and are clearly different for the three composites. When considering the two materials decomposed in H_2 and containing silver nanowires, the heating ramp during the decomposition had a crucial influence on how much silver resided in the pores upon the decomposition of the silver nitrate. Much more silver remained in the pores when a very low heating ramp of 0.1 °C min^{-1} was used (73 %), compared to when a relative high heating ramp of 1 °C min^{-1} was used (39 %). Likely, the gaseous decomposition products formed during the reduction pushed some of the silver nitrate out of the pores. By increasing the heating ramp, not only the amount of gas produced in a short time, but also the amount of mobile species increased, leading to a higher expulsion of silver nitrate. When the reduction was started at 250 °C after heating in nitrogen (Ag/SBA-15_N_2), even less silver remained in the pores (only 19%). Here, probably complete reduction of all silver nitrate took place in a very short time, allowing the formation of silver nanoparticles, but also producing large volumes of decomposition products, pushing most of the silver nitrate out of the pores.

Even though part of the silver formed large particles outside the SBA-15 pores, for all three catalysts, more than 90 % of the of silver surface atoms was located on the intraporous silver nanowires and nanoparticles. These percentages were calculated using the obtained crystallite sizes and percentages of silver present inside the pores, and the high numbers are a result of the high surface area to volume ratio of the silver nanowires and nanoparticles in comparison to the large silver particles outside of the pores. Therefore, we show the synthesis of supported silver catalysts, in which, by carefully tuning the decomposition parameters, we are able to tailor the shape of the silver and the amount of silver inside the pores of the SBA-15.

3.3. Catalysis

The supported silver catalysts (56 wt% Ag/SBA-15) were investigated for the hydrogenation of cinnamaldehyde. The reaction scheme of this reaction is given in Fig. 6. Both the C=C and the C=O bond of the α,β-unsaturated aldehyde can be hydrogenated, to form hydrocinnamaldehyde and cinnamyl alcohol, respectively. Cinnamyl alcohol (CALC) is used in the pharmaceutical, flavor and perfume industry, and is therefore the preferred product [5,35]. However, the hydrogenation of the C=C bond is thermodynamically favored [36,37], showing the need for a selective catalyst. Furthermore, hydrogenation of both the C=C and the C=O bonds, yielding hydrocinnamyl alcohol, should be avoided. Although limited in activity, silver has proven to be more selective towards cinnamyl alcohol than gold, palladium, platinum and ruthenium catalysts [35].

In Fig. 7, the conversion of cinnamaldehyde over three different Ag/SBA-15 catalysts, and the formation of products versus the reaction time is shown. The decreasing amount of cinnamaldehyde (black circles) shows that all three catalysts were active. At low conversions, mainly cinnamyl alcohol (green squares) and hydrocinnamaldehyde (orange triangles) formed, whereas hydrocinnamyl alcohol (red diamonds) started to form only after high conversion levels (> 90 %) were reached. Control experiments confirmed that without silver and upon catalyst removal, no (more) cinnamaldehyde was converted (see Supplementary Information, Fig. F1). As a reference, the reaction was run with a catalyst containing 15 wt% Ag/SBA-15 prepared via impregnation and drying (see Supplementary Information, Fig. F2).

The three catalysts clearly showed different activities and selectivities. Full conversion of cinnamaldehyde within 24 or even 7 h was reached for both catalysts containing silver nanowires (frame A and B), but not for the catalyst with the silver nanoparticles (frame C). This is partly explained by the presence of large silver crystallites in the latter, which do not contribute significantly to the catalysis. To better compare the activity of the catalysts, the turn over frequencies (TOF) for all three

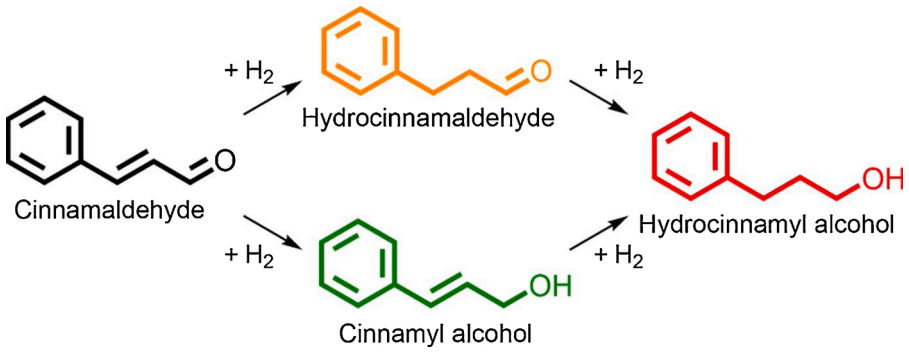

Fig. 6. Reaction scheme of cinnamaldehyde hydrogenation.

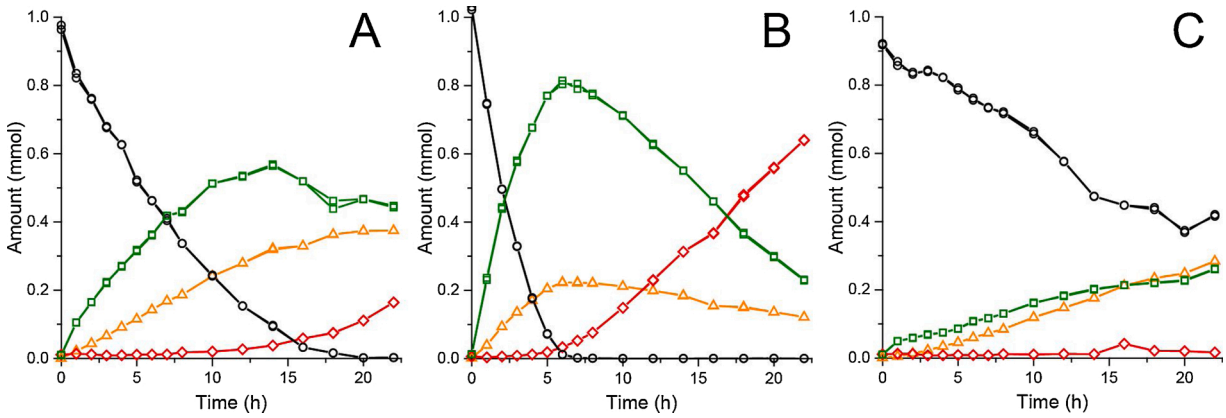

Fig. 7. Amount of cinnamaldehyde (black circles) and products, cinnamyl alcohol (green squares), hydrocinnamaldehyde (orange triangles) and hydrocinnamyl alcohol (red diamonds), during the hydrogenation of cinnamaldehyde over supported silver catalysts, Ag/SBA-15_1 (A), Ag/SBA-15_0.1 (B) and Ag/SBA-15_N_2 (C). Conditions: Cinnamaldehyde (1 mmol), catalyst (75 mg 56 wt% Ag/SiO_2, cinnamaldehyde to Ag mole ratio is 2.6), isopropanol (1 mL), H_2O (1 mL), tetradecane (100 μL), H_2 (40 bar), 70 °C, 900 rpm stirring. (For interpretation of the references to colour in the Figure, the reader is referred to the web version of this article).

catalysts and the reference catalyst prepared via impregnation and drying are listed in Table 2. These TOF values were calculated using the estimated values for the silver present inside the pores and using initial surface averaged particle diameters from TEM analysis. For the nanowires, only the surface area on the sides of the wires were taken into account. The obtained TOF values are in line with activities of silver catalysts in liquid phase hydrogenation of α,β-unsaturated aldehydes reported in literature [4,38,39].

For both the catalysts with silver nanowires, cinnamyl alcohol is the main product, whereas similar amounts of hydrocinnamaldehyde and cinnamyl alcohol are produced using Ag/SBA-15_N_2 (see Supplementary Information, Fig. G1). TEM analysis on the used catalysts (see Supplementary Information, Fig. H1) show that both catalysts containing silver nanowires were stable and retained their morphology during the hydrogenation reaction. However, this was not the case for both catalysts containing silver nanoparticles, which sintered to form significantly larger particles and nanowires. Since it is unknown when the sintering took place, no reliable conclusions for activity and selectivity based on particle size can be drawn. Still, the considerable difference in activity and selectivity between the catalyst containing nanoparticles or nanowires, suggests that large silver facets are favorable for the hydrogenation reaction, which is in agreement with literature on the hydrogenation of various unsaturated aldehydes [3,37,40].

Even though the nanoparticles were not stable, the low activity of this catalyst compared to the catalysts containing nanowires show that the silver inside the pores of the SBA-15 is active in the hydrogenation reaction, and that the activity of the silver outside of the pores can indeed be neglected. This is even further evidenced by the similar TOF values for the two catalysts containing different amount of silver nanowires. Moreover, this shows that even though the nanowires fill the pores of the SBA-15, the surfaces of the silver nanowires are accessible to the reactants. Most likely, the micropores present in the SBA-15 provide accessibility for products and reactants. This means however, that part of the surface of the silver nanowires is covered by the silica and therefore, the real active surface area is lower, and hence the real TOF values are even higher for the nanowires than reported here.

4. Conclusion

The synthesis of supported silver catalysts via melt infiltration and their application in the selective hydrogenation of cinnamaldehyde has been explored. After melt infiltration, over 90 % of the precursor, silver nitrate, was inside the pores of the SBA-15. By subsequent reduction, supported silver catalysts with a weight loading of 56 wt% were obtained. Depending on the temperature of the reduction, either silver nanowires or silver nanoparticles had formed inside the pores. However, after reduction, also some silver was located outside the pores. The external silver particles were significantly larger than those inside the pores, and could be neglected when evaluating the catalytic activity. The silver nanowires, although filling the pores of the SBA-15, were accessible for the reactants and provided more active and selective catalysts for the hydrogenation of cinnamaldehyde to cinnamyl alcohol than the silver nanoparticles.

Table 2
Catalytic properties of Ag/SBA-15 composites.

Catalyst	Shape Ag in pores	Ag in pores [%]	TOF[a] Ag in pores [mol_{CALC} $mol_{Ag,surf}^{-1}$ h^{-1}]	Selectivity to CALC at $X_{50\%}$ [%]
Ag/SBA-15_1	Nanowires	39	12	82
Ag/SBA-15_0.1	Nanowires	73	12	70
Ag/SBA-15_N_2	Nanoparticles	19	1.4	50
15Ag/SBA-15_ref	Nanoparticles	n.a.	1.0	80

[a] TOF for first hour, based on the initial surface averaged particle size determined by TEM.

CRediT authorship contribution statement

P.H. Keijzer: Methodology, Validation, Investigation, Writing - original draft, Visualization. **B. Donoeva:** Methodology, Writing - review & editing. **K.P. de Jong:** Conceptualization, Writing - review & editing, Supervision, Funding acquisition. **P.E. de Jongh:** Conceptualization, Writing - review & editing, Supervision, Funding acquisition.

Declaration of Competing Interest

The authors declare that they have no known competing financial interests or personal relationships that could have appeared to influence the work reported in this paper.

Acknowledgements

This research was funded by the Netherlands Center for Multiscale Catalytic Energy Conversion (MCEC), an NWO Gravitation programme funded by the Ministry of Education, Culture and Science of the government of the Netherlands and by a NWO-Vici grant (16.130.344). The

authors would like to thank Lee Durndell and Jovana Zečević for scientific discussions and Hans Meeldijk (TEM), Dennie Wezendonk (XRD), Marjan Versluijs-Helder (XRD), Sander Lambregts (DSC, N_2-physisorption), Jan Willem de Rijk (DSC) and Pascal Wijten (catalytic setup) for technical support.

Appendix A. Supplementary data

Supplementary material related to this article can be found, in the online version, at doi:https://doi.org/10.1016/j.cattod.2020.03.017.

References

[1] I.E. Wachs, R.J. Madix, The oxidation of methanol on a silver (110) catalyst, Surf. Sci. 76 (1978) 531–558, https://doi.org/10.1016/0039-6028(78)90113-9.
[2] M.O. Ozbek, I. Onal, R.A. Van Santen, Why silver is the unique catalyst for ethylene epoxidation, J. Catal. 284 (2011) 230–235, https://doi.org/10.1016/j.jcat.2011.08.004.
[3] P. Claus, H. Hofmeister, Electron microscopy and catalytic study of silver catalysts: structure sensitivity of the hydrogenation of crotonaldehyde, J. Phys. Chem. B 103 (1999) 2766–2775, https://doi.org/10.1021/jp983857f.
[4] X. Yang, A. Wang, X. Wang, T. Zhang, K. Han, J. Li, Combined experimental and theoretical investigation on the selectivities of Ag, Au, and Pt catalysts for hydrogenation of crotonaldehyde, J. Phys. Chem. C 113 (2009) 20918–20926, https://doi.org/10.1021/jp905687g.
[5] P. Gallezot, D. Richard, Selective hydrogenation of α,β-unsaturated aldehydes, Catal. Rev. – Sci. Eng. 40 (1998) 81–126, https://doi.org/10.1080/01614949808007106.
[6] D. Zhao, J. Feng, Q. Huo, N. Melosh, G.H. Fredrickson, B.F. Chmelka, G.D. Stucky, Triblock copolymer synthesis of mesoporous silica with periodic 50 to 300 angstrom pores, Science 279 (1998) 548–552.
[7] J.R. a Sietsma, J.D. Meeldijk, M. Versluijs-Helder, A. Broersma, A. Jos Van Dillen, P.E. de Jongh, K.P. de Jong, Ordered mesoporous silica to study the preparation of Ni/SiO_2 ex nitrate catalysts: impregnation, drying, and thermal treatments, Chem. Mater. 20 (2008) 2921–2931, https://doi.org/10.1021/cm702610h.
[8] J.R.A. Sietsma, H. Friedrich, A. Broersma, M. Versluijs-Helder, A. Jos van Dillen, P. E. de Jongh, K.P. de Jong, How nitric oxide affects the decomposition of supported nickel nitrate to arrive at highly dispersed catalysts, J. Catal. 260 (2008) 227–235, https://doi.org/10.1016/j.jcat.2008.10.007.
[9] R.M. Rioux, H. Song, J.D. Hoefelmeyer, P. Yang, G.A. Somorjai, High-surface-area catalyst design: synthesis, characterization, and reaction studies of platinum nanoparticles in mesoporous SBA-15 silica, J. Phys. Chem. B 109 (2005) 2192–2202, https://doi.org/10.1021/jp048867x.
[10] A. Martínez, C. López, F. Márquez, I. Díaz, Fischer-Tropsch synthesis of hydrocarbons over mesoporous Co/SBA-15 catalysts: the influence of metal loading, cobalt precursor, and promoters, J. Catal. 220 (2003) 486–499, https://doi.org/10.1016/S0021-9517(03)00289-6.
[11] S. Singh, R. Kumar, H.D. Setiabudi, S. Nanda, D.V.N. Vo, Advanced synthesis strategies of mesoporous SBA-15 supported catalysts for catalytic reforming applications: a state-of-the-art review, Appl. Catal. A Gen. 559 (2018) 57–74, https://doi.org/10.1016/j.apcata.2018.04.015.
[12] J.E. van den Reijen, S. Kanungo, T.A.J. Welling, M. Versluijs-Helder, T.A. Nijhuis, K.P. de Jong, P.E. de Jongh, Preparation and particle size effects of Ag/α-Al_2O_3 catalysts for ethylene epoxidation, J. Catal. 356 (2017) 65–74, https://doi.org/10.1016/j.jcat.2017.10.001.
[13] P. Munnik, P.E. de Jongh, K.P. de Jong, Recent developments in the synthesis of supported catalysts, Chem. Rev. 115 (2015) 6687–6718, https://doi.org/10.1021/cr500486u.
[14] M. Wolters, L.J.W. Van Grotel, T.M. Eggenhuisen, J.R.A. Sietsma, K.P. de Jong, P. E. de Jongh, Combining confinement and NO calcination to arrive at highly dispersed supported nickel and cobalt oxide catalysts with a tunable particle size, Catal. Today 163 (2011) 27–32, https://doi.org/10.1016/j.cattod.2010.02.052.
[15] C.E. Pompe, M. Slagter, P.E. de Jongh, K.P. de Jong, Impact of heterogeneities in silica-supported copper catalysts on their stability for methanol synthesis, J. Catal. 365 (2018) 1–9, https://doi.org/10.1016/j.jcat.2018.06.014.
[16] E. Plessers, J.E. van den Reijen, P.E. de Jongh, K.P. de Jong, M.B.J. Roeffaers, Origin and abatement of heterogeneity at the support granule scale of silver on silica catalysts, ChemCatChem 9 (2017) 4562–4569, https://doi.org/10.1002/cctc.201700753.
[17] E. Plessers, I. Stassen, S.P. Sree, K.P.F. Janssen, H. Yuan, J. Martens, J. Hofkens, D. De Vos, M.B.J. Roeffaers, Resolving interparticle heterogeneities in composition and hydrogenation performance between individual supported silver on silica catalysts, ACS Catal. 5 (2015) 6690–6695, https://doi.org/10.1021/acscatal.5b02119.
[18] P. Munnik, N.A. Krans, P.E. De Jongh, K.P. De Jong, Effects of Drying Conditions on the Synthesis of Co/SiO_2 and Co/Al_2O_3 Fischer – Tropsch Catalysts, ACS Catal. 4 (2014) 3219–3226.
[19] P.E. de Jongh, T.M. Eggenhuisen, Melt infiltration: an emerging technique for the preparation of novel functional nanostructured materials, Adv. Mater. 25 (2013) 6672–6690, https://doi.org/10.1002/adma.201301912.
[20] C. Ciotonea, B. Dragoi, A. Ungureanu, C. Catrinescu, S. Petit, H. Alamdari, E. Marceau, E. Dumitriu, S. Royer, Improved dispersion of transition metals in mesoporous materials through a polymer-assisted melt infiltration method, Catal. Sci. Technol. 7 (2017) 5448–5456, https://doi.org/10.1039/c7cy00963a.
[21] Y.M. Wang, Z.Y. Wu, L.Y. Shi, Rapid functionalization of mesoporous materials: directly dispersing metal oxides into as-prepared SBA-15 occluded with template, Adv. Mater. 15 (2005) 323–327, https://doi.org/10.1002/adma.200400860.
[22] T.M. Eggenhuisen, H. Friedrich, F. Nudelman, J. Zec, N.A.J.M. Sommerdijk, P.E. de Jongh, K.P. de Jong, Controlling the distribution of supported nanoparticles by aqueous synthesis, Chem. Mater. 25 (2013) 890–896.
[23] T.M. Eggenhuisen, J.P. den Breejen, D. Verdoes, P.E. de Jongh, K.P. de Jong, Fundamentals of melt infiltration for the preparation of supported metal catalysts. The case of Co/SiO_2 for Fischer-Tropsch Synthesis, J. Am. Chem. Soc. 132 (2010) 18318–18325, https://doi.org/10.1016/j.cattod.2010.02.052.(41).
[24] M.Y. Wang, Z.Y. Wu, H.J. Wang, J.H. Zhu, Fabrication of metal oxides occluded in ordered mesoporous hosts via a solid-state grinding route: the influence of host – guest interactions, Adv. Funct. Mater. 16 (2006) 2374–2386, https://doi.org/10.1002/adfm.200500613.
[25] S. Yang, W. Su, S.D. Lin, J. Rick, J. Cheng, J. Liu, C. Pan, D. Liu, J. Lee, T. Chan, H. Sheu, B. Hwang, Preparation of nano-sized Cu from a rod-like $CuFe_2O_4$: suitable for high performance catalytic applications, Appl. Catal. B Environ. 106 (2011) 650–656, https://doi.org/10.1016/j.apcatb.2011.06.030.
[26] L.M. Worboys, P.P. Edwards, P.A. Anderson, Silver nanowires: inclusion in and extrusion from a mesoporous template, Chem. Commun. 2 (2002) 2894–2895, https://doi.org/10.1039/b209126g.
[27] H.I. Lee, J.H. Kim, G.D. Stucky, Y. Shi, C. Pak, J.M. Kim, Morphology-selective synthesis of mesoporous SBA-15 particles over micrometer, submicrometer and nanometer scales, J. Mater. Chem. 20 (2010) 8483–8487, https://doi.org/10.1039/c0jm00820f.
[28] K.H. Stern, High temperature properties and decomposition of inorganic salts part 3, nitrates and nitrites, J. Phys. Chem. Ref. Data 1 (1972) 747–772, https://doi.org/10.1063/1.3253104.
[29] G.H. Findenegg, S. Jähnert, D. Akcakayiran, A. Schreiber, Freezing and melting of water confined in silica nanopores, Chem. Phys. Chem. 9 (2008) 2651–2659, https://doi.org/10.1002/cphc.200800616.
[30] R.L. Oliveira, M. Shakeri, J.D. Meeldijk, K.P. de Jong, P.E. de Jongh, Mapping nanocavities in plugged SBA-15 with confined silver nanostructures, Microporous Mesoporous Mater. 201 (2015) 234–239, https://doi.org/10.1016/j.micromeso.2014.09.026.
[31] C. de Mello Donegá, P. Liljeroth, D. Vanmaekelbergh, Physicochemical evaluation of the hot-injection method, a synthesis route for monodisperse nanocrystals, Small 1 (2005) 1152–1162, https://doi.org/10.1002/smll.200500239.
[32] P. Scherrer, Bestimmung der inneren Struktur und der Größe von Kolloidteilchen mittels Röntgenstrahlen, Kolloidchem. Ein Lehrb. 277 (1912) 387–409, https://doi.org/10.1007/978-3-662-33915-2_7.
[33] J.I. Langford, A.J.C. Wilson, Scherrer after sixty years: a survey and some new results in the determination of crystallite size, J. Appl. Crystallogr. 11 (1978) 102–113, https://doi.org/10.1107/S0021889878012844.
[34] V. Uvarov, I. Popov, An estimation of the correctness of XRD results obtained from the analysis of materials with bimodal crystallite size distribution, CrystEngComm 17 (2015) 8300–8306, https://doi.org/10.1039/c5ce01799h.
[35] Y. Yuan, S. Yao, M. Wang, S. Lou, N. Yan, Recent progress in chemoselective hydrogenation of α,β-unsaturated aldehyde to unsaturated alcohol over nanomaterials, Curr. Org. Chem. 17 (2013) 400–413.
[36] M.A. Vannice, B. Sen, Metal-support effects on the intramolecular selectivity of crotonaldehyde hydrogenation over platinum, J. Catal. 115 (1989) 65–78, https://doi.org/10.1016/0021-9517(89)90007-9.
[37] P. Claus, Selective hydrogenation of α,β-unsaturated aldehydes and other C=O and C=C bonds containing compounds, Top. Catal. 5 (1998) 51–62, https://doi.org/10.1023/A:1019177330810.
[38] E. Plessers, D.E. De Vos, M.B.J. Roeffaers, Chemoselective reduction of α,β-unsaturated carbonyl compounds with UiO-66 materials, J. Catal. 340 (2016) 136–143, https://doi.org/10.1016/j.jcat.2016.05.013.
[39] P.G.N. Mertens, P. Vandezande, X. Ye, H. Poelman, I.F.J. Vankelecom, D.E. De Vos, Recyclable Au0, Ag0 and Au0-Ag0 nanocolloids for the chemoselective hydrogenation of α,β-unsaturated aldehydes and ketones to allylic alcohols, Appl. Catal. A Gen. 355 (2009) 176–183, https://doi.org/10.1016/j.apcata.2008.12.013.
[40] H. Wei, C. Gomez, J. Liu, N. Guo, T. Wu, R. Lobo-Lapidus, C.L. Marshall, J. T. Miller, R.J. Meyer, Selective hydrogenation of acrolein on supported silver catalysts: A kinetics study of particle size effects, J. Catal. 298 (2013) 18–26, https://doi.org/10.1016/j.jcat.2012.10.027.